OPEN ACCESS
IOP Publishing
Measurement Science and Technology
Meas. Sci. Technol. **35** (2024) 095016 (16pp)
https://doi.org/10.1088/1361-6501/ad4fae

Measurement of Si pixel sensor alignment for the ALICE ITS detector

Ahmad Satya Wicaksana[1,2], **Esa Prakasa**[1,*], **Antonio Di Mauro**[3] and **Siswo Wardoyo**[2]

[1] Research Center for Data and Information Sciences, Research Organization for Electronics and Informatics, Indonesian National Research and Innovation Agency (BRIN), Bandung, Indonesia
[2] Department of Electrical Engineering, Faculty of Engineering, University of Sultan Ageng Tirtayasa, Cilegon, Indonesia
[3] European Organization for Nuclear Research (CERN), Geneva, Switzerland

E-mail: esap001@brin.go.id

Received 6 April 2023, revised 2 May 2024
Accepted for publication 23 May 2024
Published 25 June 2024

Abstract

A Large Ion Collider Experiment (ALICE) experiment is one of the four experiments at the Large Hadron Collider (LHC) designed to investigate the status of matter under very high energy densities produced during heavy-ion collisions. The ALICE inner tracking system (ITS) consists of seven concentric cylindrical layers of monolithic silicon pixel sensors known as ALICE pixel detector (ALPIDE). The sensors are used to reconstruct the paths of charged particles generated in the collisions. The sensor alignment of the detector must be adjusted to a high precision standard. The adjustment objective is to obtain a detector that can undertake high-resolution measurements. This paper introduces a method for measuring the reference markers utilized in sensor alignment determination. Markers engraved at the chip corners have been detected using the Hough transform, Canny edge detection, and template matching techniques. The distances between two markers are measured to determine the accuracy of the pixel sensor alignment before and after assembly. The proposed methods exhibit an accuracy exceeding 99% and demonstrate high speed analysis. The average processing times for detecting the circle and cross markers are 105.9 ms/image and 113.8 ms/image, respectively. The sensor alignment of the detector must be adjusted to a high precision standard. However, recent studies have shown deviations of up to 5 μm above the desired value in the measured sensor position. Such deviations do not represent a major issue, nevertheless it is important to measure them in order to speed-up and make more accurate the recursive track-based alignment procedure used to reconstruct the position of each pixel sensor in the tracking detector. The proposed method offers a promising solution to deliver precise and rapid measurements for a large number of examined objects.

Keywords: visual inspection, object detection, Hough transform, Canny edge detection, template matching

* Author to whom any correspondence should be addressed.

1. Introduction

A Large Ion Collider Experiment (ALICE) is a multi-purpose heavy ion detector at European Organization for Nuclear Research (CERN), which aims to study the status of matter at the extremely high energy densities and temperatures reached in heavy-ion collisions. A high-standard measurement instrument is required to ensure the experiment data can be accurately collected. The experiment uses a detector that is composed of many silicon-based sensors. For multiple reasons, it is important that visual inspection be incorporated into the production process of chip-based detectors, like the ALICE pixel detector (ALPIDE) sensors used in the ALICE experiment. The first aspect is the quality assurance of the manufacturing process. The main method for protecting against manufacturing flaws is visual inspection. Early detection of anomalies, such as physical damage, improper reference points, irregular component placement, or manufacturing errors, guarantees that only high-quality detectors move on to the next phase of the process. This is particularly important when producing precision instruments, such as detectors based on chips, because even small flaws can affect the measurement results.

The second aspect is alignment verification. Visual inspection plays a vital role in verifying the correct alignment of components. In the case of chip-based detectors, where precise alignment is essential for accurate particle trajectory reconstruction, visual inspection ensures that each component is positioned according to specifications. Misalignments or deviations can be identified and corrected before the detector is assembled, contributing to the overall accuracy of the detector. A third aspect relates to the detection and calibration of markers. Reference markers are an essential component in the process of establishing sensor alignment. With the assistance of techniques for image processing such as the Hough transform and template matching, these markers can be accurately discovered within visual inspection. By performing this procedure, the detector can be calibrated and its components can be positioned with the required precision.

The last aspect concerns the detection and correction of errors. Visual inspection serves as a means to identify errors or inconsistencies that may arise during the manufacturing process. Visual inspection enables the timely identification of various issues, including but not limited to variations in the materials used in production, defects introduced during the fabrication process, and problems encountered during assembly. This early identification facilitates timely corrections, preventing the production of faulty detectors and minimizing the need for rework. In brief, visual inspection is an essential part of the chip-based detector manufacturing process, serving as a critical element in ensuring quality control, verifying alignment, and identifying errors. The implementation of this system guarantees that the detectors satisfy the high standards that are essential for precise and consistent scientific measurements.

The paper will report the implementation of a visual inspection of the chip sensor installation on the ALICE inner tracking system (ITS) detector. The ALICE ITS detector modules are composed of a hybrid integrated circuit (HIC), assembled by gluing a flexible printed circuit (FPC) on top of nine sensor chips aligned by an automated pick and place machine with a precision of $\pm 5\,\mu$m. The sensor chip arrangement needs to be mounted precisely on the support component. The precise installation aims to obtain high resolution on the reconstructed trajectories of the charged particles that are produced in the collision and traverse the ITS detectors. Therefore, this work is the initial step to ensure the quality of the data samples that will be collected. The accurate placement of the sensor chips on the assembly vacuum table is obtained by using a vision system and reference markers (circles at each position on the vacuum table, and crosses at the four corners of the sensor chips).

Our research novelty includes two aspects: firstly, the proposed methods can provide highly accurate measurements in the implementation of assembly procedures for sensor chips. Secondly, we can conduct the measurement at high speeds without requiring a high computational load. The method consists of two main tasks: circle and cross-marker detection. Both detections have processing times of only around 100 ms per image, respectively. The image scaling ratio is critical to reducing computing costs while maintaining accuracy levels.

The image analysis-based measurement is important because it speeds up and provides a more accurate alignment status than the recursive track-based alignment procedure. This procedure is the current standard for reconstructing the position of each pixel sensor in the tracking detector. The proposed method can provide a general view of chip alignment prior to the detector's installation stages. The proposed method performs the measurement analysis based on the image data obtained from direct acquisition of the camera from the chip surfaces. Therefore, the proposed method directly computes the distance parameters using the image data from the chip surfaces. The measurement is not calculated based on the indirect parameters. Image processing methods present significant advantages when measuring objects on the scale of micrometers and millimeters [1]. One essential advantage of employing image processing algorithms is their attainable precision. The technique can analyze images at the pixel level to determine detailed distances. Furthermore, the image analysis approach allows for non-contact measurement, preventing the risk of physical destruction to the observed object. Various inspection procedures could apply these principles to obtain high-quality measurements.

This paper, which consists of five sections, can be described as follows. The context and purpose of the research work are explained in section 1 of the paper. Section 2 mentions several previous works. Section 3 discusses and explains the data acquisition and analysis methods used in this research work. The results of the algorithms and the discussion on their performance are presented in section 4. Section 5 contains the paper's conclusion.

2. Previous works

Object detection is widely applied in industry applications, such as defect detection of electrical components or printed circuit boards (PCBs) [2]. As demands in PCB process design and quality assurance escalate, the diversity of defects found on PCB surfaces, including spurs, mouse bites, short circuits, and open circuits, continues to expand. Consequently, there is a corresponding increase in the need for enhanced detection accuracy to meet these evolving quality standards [3, 4]. Experts are required to manually examine the devices, with each sample taking a considerable amount of time. Any differences from the original blueprints must be spotted and evaluated [5].

Yeum and Dyke [6] describes a combination of edge detection and template matching for visual inspection of bridges. The method demonstrated success in identifying damage to bridge structures without controlling the angle or position of the images, simulating real-world scenarios. However, challenges may arise in situations with fluctuating lighting conditions inherent in received image datasets. In [7], the application of Hough transform and template matching methods for defect detection during the etching process on PCBs yielded promising results. However, limitations became evident in scenarios of subpar image quality, including challenges such as inadequate lighting, variations in height during image capture, and image skew. These constraints pose difficulties for the framework when processing images with such quality issues, highlighting the necessity for enhancements to address diverse image conditions. This is especially crucial when compared to template matching-based reference methods and manual detections, which suffer from drawbacks such as inefficient defect detection, substantial errors in defect identification and localization, and limited adaptability of detection techniques [8].

Nan and Gao [9] presents automated detection methods for inspecting the condition of the brake beam bolt. This component is an important locking part of the train components and needs to be inspected regularly to ensure quality and safety. For the bolt position detection, the template matching method was employed, and afterwards, support vector machines were used to classify the condition of the railroad tracks based on the position of the bolt. The accuracies obtained for joint part localization and fault detection are 99% and 95%, respectively. In [10], five edge detection methods in image processing are compared, namely Canny edge detection, Sobel edge detection, Prewitt edge detection, Robert edge detection, and zero crossing edge detection. The result is that Canny edge detection provides higher accuracy compared to the other four methods.

Panjaitan *et al* [11] applies the Hough transform, Canny edge detection, and template matching algorithms to detect sealring, edge, and cross markers on sensor chips. The results of the object detection are used to determine the quality of chip cutting. The obtained accuracy is 97%. In [12], template matching and fast Fourier transform methods were used to detect defects in the electronic surface. The obtained accuracy is 100% and requires less time. The limitation of this paper is that the templates used in the method are not comprehensive or fail to capture the full range of possible defects.

Yang and Sun [13] proposes a convolutional neural network (CNN) method for detecting semiconductor defects. The result of that object detection provides higher accuracy but requires significant power processing and more time to operate. In [14], the limitations of traditional surface defect detection algorithms in industrial applications and present the state-of-the-art in surface defect inspection using deep learning, focusing on semiconductor, steel, and fabric manufacturing processes. The advantages of deep learning, particularly in one-stage defect detection, automatic feature learning, and robustness to input variations, are highlighted [15]. Despite these advantages, challenges such as insufficient labeled training data, real-time processing requirements, and the need for innovative algorithms persist. The study suggests that with advancements in data augmentation, semi-supervised learning, and efficient convolution algorithms, deep learning has the potential to replace traditional defect detection methods, offering a promising future for surface defect inspection in industrial settings.

As described in [16], the hybrid multi-stage system of stacked deep neural networks offers substantial advancements in automated visual fault inspection. The inspection detects minute defect patterns within high-resolution imagery, with runtime of only 5.2 ms per chip image sample. The results demonstrate superior performance, with an F_1-score of up to 99.5%, showcasing the potential of this approach to surpass current state-of-the-art automated visual inspection methods while meeting runtime constraints in real-time processing.

Jia *et al* [17] investigates the application of deep learning for automated defect detection in smart manufacturing, highlighting its strengths and weaknesses. Deep learning proves beneficial in overcoming the limitations of traditional image processing techniques, particularly in handling background noise and texturing variations. The study emphasizes the growing significance of deep learning in defect detection, citing its strength in coping with complex tasks. However, challenges include the scarcity of defect data for effective implementation and the inherent complexity of deep learning models, which pose difficulties in comprehending and explaining decision-making processes, thereby hindering deployment and performance enhancement.

Apostolopoulos and Tzani [18] focuses on the need for advanced defect detection in smart manufacturing by proposing a specialized CNN named multipath VGG19 (MVGG19). Utilizing six industrial image datasets, MVGG19, a modified version of the VGG19 network, outperforms the baseline in five datasets, demonstrating improved accuracy and robustness. The proposed architecture not only contributes an innovative modification to VGG19 for defect and industrial object recognition but also establishes itself as a baseline model with potential applications in various manufacturing domains. However, a notable limitation of this study is the imbalance observed between datasets containing defected materials and those focused on actual object recognition.

Ren *et al* [19] provides a comprehensive overview of the role of machine vision in industrial inspection, emphasizing

its significant contributions to efficiency, quality, and reliability. The discussion covers the history and current state of optical illumination, image acquisition, image processing, and image analysis, with a particular focus on the growing impact of deep learning in defect detection. Despite notable achievements, challenges remain, including the need for real-time inline detection for objects with complex features, addressing interference in detection systems, dependency on large-scale datasets, and enhancing the intelligence level of vision systems. The study concludes that, despite existing imperfections, machine vision remains a crucial direction for future research and development in defect detection.

Cai and Gong [20] investigates that inspecting FPC Boards (FPCBs) is crucial in manufacturing activities, yet edge detection for Region of Interest (ROI) poses challenges. This study introduces a segmentation method targeting the gold finger area of FPCBs, addressing adhesion concerns. The approach involves Gaussian filtering, generating a blurred edge image, creating a binary image using adaptive thresholding, and extracting the gold finger area using histogram statistics. Experimental results demonstrate accurate gold finger area localization, with the algorithm processing taking 2.654 s with adaptive thresholding and 1.442 s without, making it suitable for automated optical inspection of FPCBs.

Chen *et al* [21] addresses the challenges in PCB defect detection, such as high costs and complex shapes. This study proposes a novel approach combining image processing and deep learning. By employing the pruned YOLOv5 algorithm and various image enhancement techniques, including straightening, denoising, sharpening, and contrast enhancement, the method enhances defect identification and localization on PCB boards, leading to improved detection accuracy. However, it is worth noting that this approach may require significant computational resources, utilizing CPU: AMD R7-5800H and GPU: NVIDIA GeForce RTX 3060, for efficient processing. Nonetheless, experimental results demonstrate promising outcomes, including model compression to 2.64 MB and inference time reduction to 20.53 ms, significantly enhancing deployment efficiency and detection speed.

The contribution of automated functions to smart manufacturing is described in [22]. The operation comprises information perception and decision-making, and relies heavily on sensor data, with image recognition serving as a critical component. Leveraging deep learning architectures, such as YOLO models, offers efficient image analysis in automated environments. Despite its advantages, this approach may require substantial computational resources. The study primarily focuses on YOLOv3 models, which achieve promising accuracy rates, especially when combined with data augmentation techniques. However, limitations arise from the specificity of the collected image data and the need for more diverse datasets and innovative models for future studies. Additionally, while the region-based convolutional neural network (R-CNN) model shows excellent image recognition results, it requires extensive data for training, highlighting the importance of automatic correction mechanisms to enhance learning outcomes. Further exploration into image preprocessing methods, including binary image processing, may also improve data quality and model performance in future research endeavors.

In contrast to the discussion on YOLOv3 and R-CNN models, this study focuses on enhancing the YOLOv8-based method for PCB defect identification. While YOLOv3 models have been pivotal in achieving promising accuracy rates, especially when combined with data augmentation techniques, the study introduces the YOLOv8s model to address the challenge of detection speed. By implementing the CA attention mechanism for improved feature extraction, the enhanced YOLOv8s-CA algorithm exhibits significant advancements: a footprint of 5.79 MB, a mean average precision of 90.4%, and a minimal parameter count increase. This highlights the potential of the YOLOv8s-CA model for compact industrial inspection systems and various applications, showcasing advancements over traditional models like YOLOv3 [23].

3. Methodology

Our research focuses on image processing tasks involving object detection and distance measurement. We used the ALPIDE dataset, which contains 208 high-resolution images with objects of interest. This dataset was specifically chosen for its suitability for tasks involving the Hough transform, Canny edge detection, template matching, and subsequent distance measurement.

Figure 1 shows two aligned chips on top of the module assembly machine (MAM)[4] table and a view of the back-side of a HIC with nine aligned sensors [24]. A detailed explanation of the research objects shown in figure 1 is given as follows. The microscopic camera (No. 1) is installed above the chip surfaces (No. 2). The chips are laid on the assembly table (No. 3). A total of nine sensor chips (No. 4) are constructed to form an integrated circuit (No. 5).

The name of the camera is Basler Ace Ethernet Camera. It has a resolution of $2,048 \times 2,048$ pixels. In the optic part, the lens is a navitar assembly. The microscope is equipped with a $10\times$ microscope objective and connected with a coaxial LED illuminator. The field of view of the camera is 1.1 mm. The image acquisition is in an enclosed area that can minimize the interference of the environmental illumination. This camera arrangement provides a spatial resolution of 0.54 μm per pixel. For a comprehensive overview of the camera specifications, please refer to table 1.

In the work presented in this paper, we applied various image processing techniques to enhance the analysis of sensor chip images. Initial preprocessing steps, such as noise reduction, contrast enhancement, and resizing, were conducted to optimize the dataset. For object detection, we employed a multi-step strategy involving the Hough transform, Canny

[4] The assembly machine is supplied by IBS Precision Engineering, Netherlands.

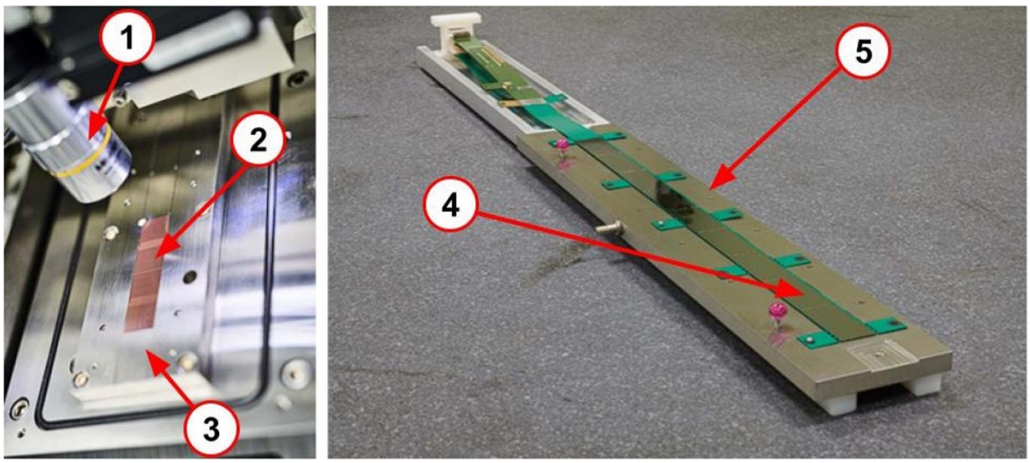

Figure 1. Left: Two aligned chips on the module assembly machine table. Right: The back-side of a HIC with nine aligned sensor chips.

Table 1. Basler camera specification.

Specification	Description
Resolution	1838.2 px mm^{-1}
Spatial resolution	0.54 µm/px
Pixels	2048 px
Gain	50
Exposure time	30 µm s^{-1}
Frame rate	20 frame s^{-1}
Light source intensity	12%
Field of view	1.1 mm

edge detection, and template matching methods. These techniques were specifically employed to identify the circle marker on the assembly vacuum table and the cross marker on the sensor chips. The precise positions of these markers along horizontal and vertical coordinates were determined to assess the accuracy of sensor alignment in the ITS Inner Barrel modules. Reference markers, exemplified in images A and B of the left and right corners of the sensor chip in figure 2, played a crucial role in this alignment verification process.

The algorithm presented in this work has three main processes: (i) circle marker detection using Hough transform and Canny edge detection; (ii) cross marker detection using the template matching method; and (iii) measurement of the vertical and horizontal distance between the circle and the cross markers to characterize the chip alignment. A picture of the reference markers that should be measured is reported in figure 3.

This work used the main hardware device with the following specifications:

- Processor: AMD Ryzen 5 Mobile 2500U
- Graphics: AMD Radeon™ Vega 8 Graphics
- Memory: 8192 MB RAM

The algorithm was facilitated by employing Visual Studio Code 1.59.1, integrated with Python 3.9.1. This research made use of the following Python packages: OpenCV2 v4.5.1, Numpy v1.19.3, Scikit-image v0.18.1, and Matplotlib v3.3.3. These algorithms for circle and cross marker detection were conducted with the specific parameters outlined in table 2.

3.1. Circle and cross marker detection

For the application presented in this paper, the algorithm to find the position of the circle marker begins by resizing the image using a scale ratio of 0.2. Then, the image is converted to gray scale and an image segmentation with eight threshold levels is performed. According to [25], reducing the resolution of an image or frame of videos can improve the computational efficiency of the model to some extent. The use of eight threshold levels is motivated by the fact that for several sensor chips, the circle markers are not detected at a certain level. If several (fake) circles are detected for a given threshold level, then the circle marker radius is fixed in the detection algorithm to the value of 38 pixels (corresponding to the expected radius of 190 pixels in the original image before scaling) with a tolerance of 2 pixels.

After applying an average filter and an opening morphological transformation with a kernel size of 8×8, which are aimed at smoothening the image or reducing the noise caused by the threshold [26, 27], the Canny edge detection and the circular Hough transform are used to detect and automatically determine the circle marker position. Once the position is known, the centroid of the circle marker is calculated. The detection algorithm is applied for each of the eight threshold levels, and an average value of the circle marker position is computed considering the threshold levels for which the measured marker radius is consistent with the expected value. The methods used in this study are schematized in the flowchart in figure 4.

In our methodology, scaling plays a pivotal role in addressing variations in object size within input images. To achieve this, our template matching algorithm incorporates a scaling method that systematically reduces the size of the template image. Specifically, this scaling approach ensures that

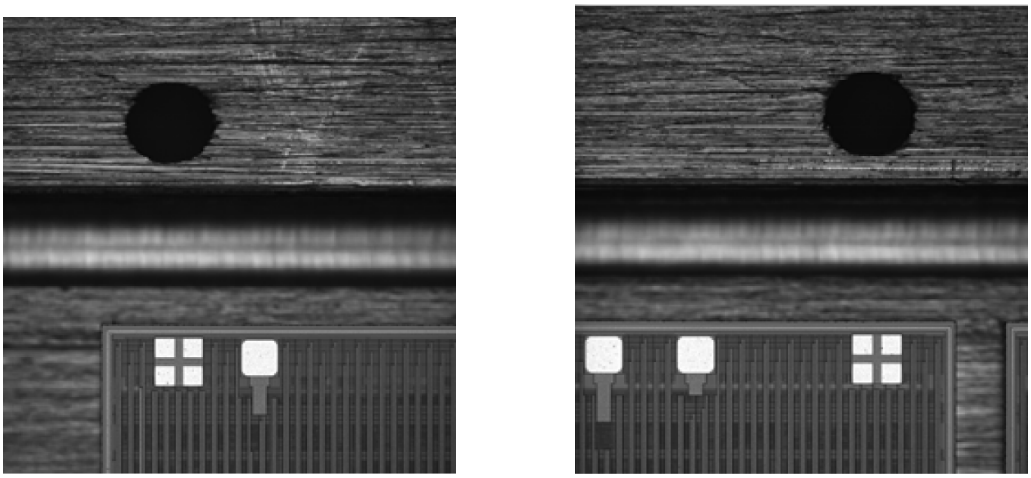

(a) Image A (b) Image B

Figure 2. The microscopic images of sensor chips: (a) Left side sensor chip. (b) Right side sensor chip.

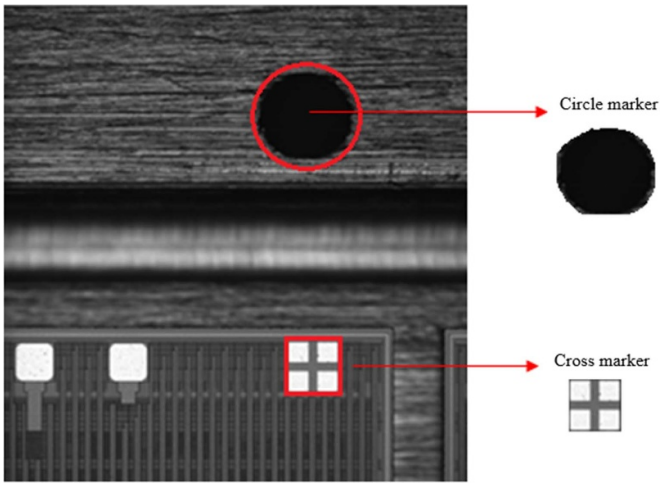

Figure 3. Example of the reference markers to be measured.

Table 2. Parameters for image processing techniques.

Technique	Parameter	Value
Hough transform	Detection method	Hough gradient
	Resolution ratio	1
	Minimum distance of two circles	20 pixels
	Upper threshold intensity	50
	Threshold intensity for circle detection	30
	Minimum and maximum circle radius	0 pixels (the radius before detection is not available)
Canny edge detection	Lower threshold intensity	100
	Higher threshold intensity	200
Template matching	Template image	41 × 41 pixels
	Pad input	True
	Peak local maximum with threshold	0.8

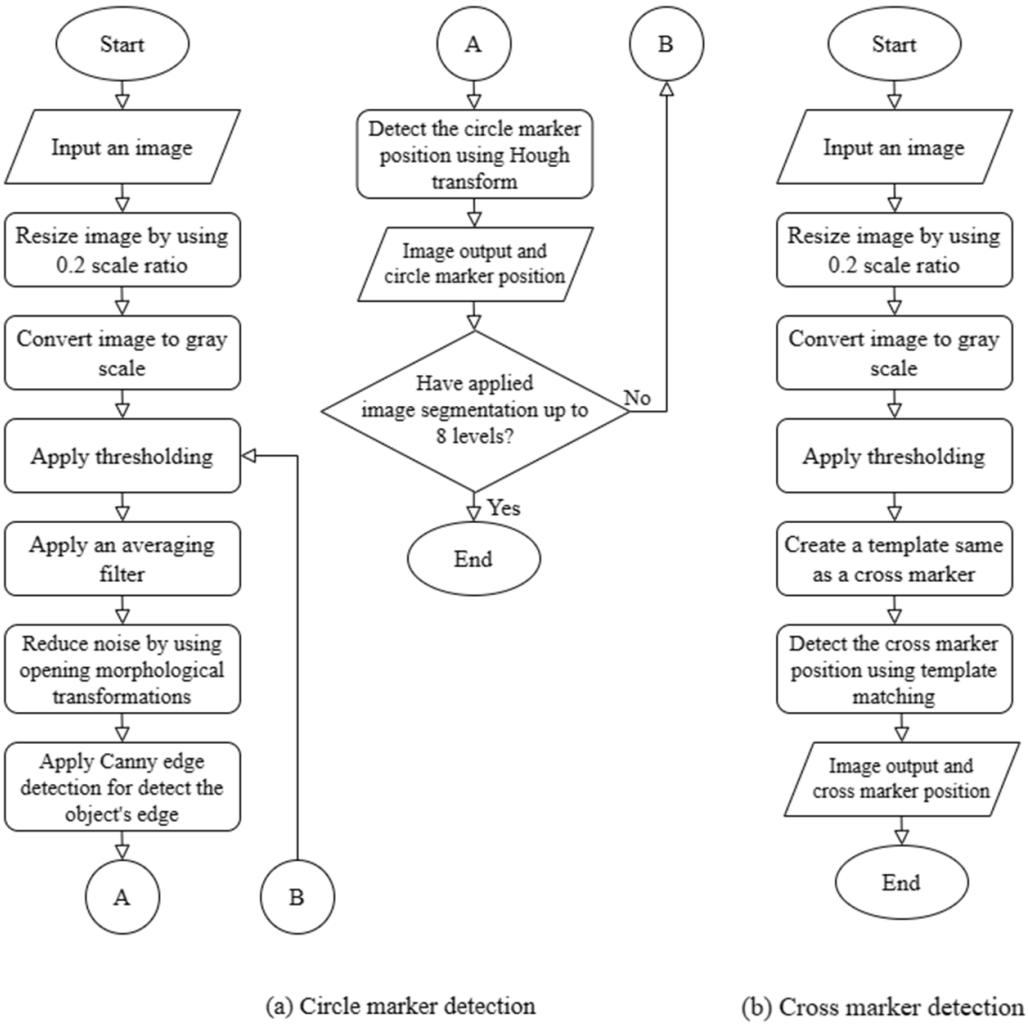

Figure 4. Object detection flowchart.

the template is approximately 20% smaller than the original object, thereby enhancing our capacity to effectively handle diverse object sizes encountered in input images.

Template matching involves a meticulous process of creating a representative template image. This is achieved through the extraction of key features from the object of interest, followed by the generation of a matrix representation. The resulting template image is intricately crafted to faithfully represent the object, ensuring its suitability for robust matching in various scenarios.

The coordinates of the cross marker are defined by the position of the input template that provides the best match to the marker in the image being processed. This position is marked by the highest intensity. Once this position is known, the centroid's value of the cross marker is displayed in the terminal output, as shown in figure 5.

It is important to note a deliberate omission in our methodology-noise handling. This intentional exclusion is motivated by the potential impact of noise on the pixel values of the template image. By opting not to address noise in our approach, we aim to preserve the integrity of the template's representation, prioritizing accuracy and reliability in the context of robust matching.

3.2. Distance measurement

Before calculating the distance between the circle and the cross markers along the horizontal and vertical axes, we should rescale the position of the detected centroid to properly define the ROI of the circle and the cross markers at 100% scale. The coordinates (expressed in units of pixels) along the vertical axis of the circle and the cross markers are denoted by iC and iR, while the horizontal coordinates are indicated as jC and jR, as shown in figure 6. The values of D_X and D_Y denote the horizontal and vertical distances (expressed in μm) between the circle and the cross markers, respectively.

$$D_X = (jR - jC)\ \text{px} \times 0.544\ \mu\text{m/px} \tag{1}$$

$$D_Y = (iR - iC)\ \text{px} \times 0.544\ \mu\text{m/px} \tag{2}$$

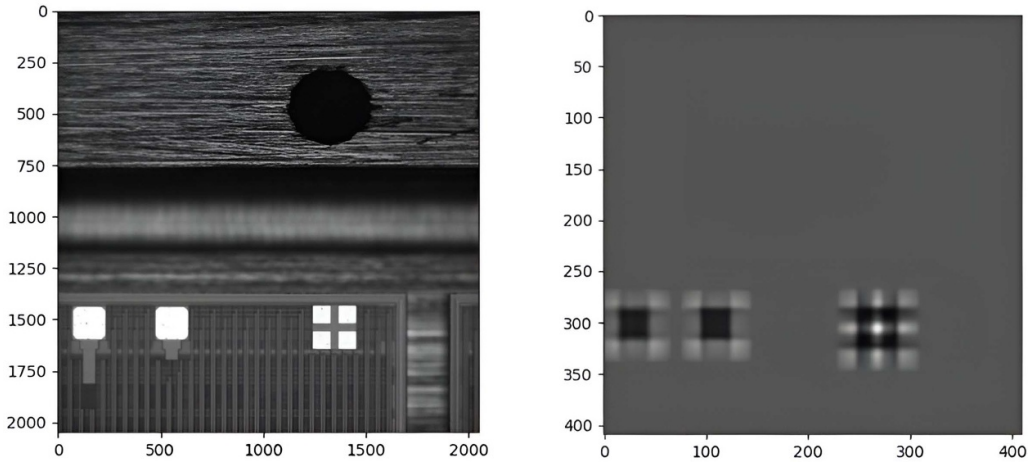

Figure 5. Display of the cross marker centroid value.

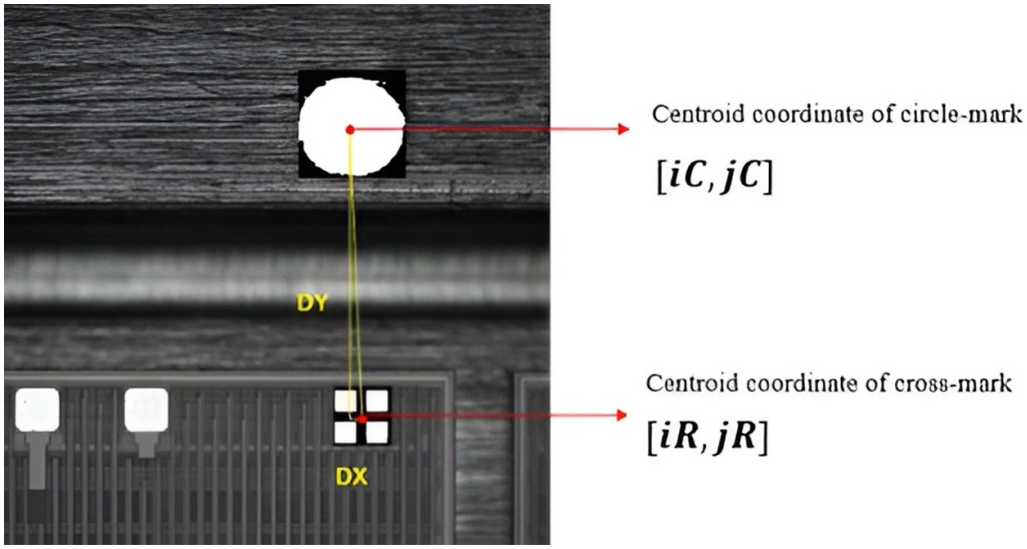

Figure 6. Centroid coordinate of the circle and the cross markers.

As shown in equations (1) and (2), the circle marker is used as the reference position. The horizontal distance D_X between the cross and the circle markers will be negative if the cross marker is located on the left side of the circle-marker. Conversely, the D_X will be positive if the cross marker is on the right side of the circle-marker, as shown in figure 7.

After the distances between the circle and the cross markers of the chip are determined, the horizontal distance (D_X) is used to measure the inter pixel distance (IpD) from a single sensor chip to another chip in the same HIC according to:

$$IpD = 30.150\,mm - \frac{D_{Xn}\,\text{chip}}{1000}\,mm + \frac{D_{Xn+1}\,\text{chip}}{1000}\,mm. \quad (3)$$

As illustrated in figure 8, the horizontal distance between the cross markers in the left and right corners of adjacent chips is intended to be 30.150 mm. The values of IpD characterize the chip alignment. These values should be in accordance with the standard deviation (5 µm) required for the assembly procedure [24]. The accuracy (expressed in percentage) is obtained by comparing the IpD values between references and measurements, according to:

$$Accuracy = \left(1 - \left|\frac{\text{Measured} - \text{Reference}}{\text{Reference}}\right|\right) \times 100\% \quad (4)$$

4. Results and discussion

The algorithms described in section 3 have been tested on twelve HICs. A HIC consists of nine chips, and each chip has two associated images, namely image A (left side) and image B (right side) of the sensor chips, as shown in figure 2. The algorithm is able to detect the position of the circle and the cross markers of each HIC precisely and accurately, although each image has a different quality, as shown in figure 9. The average processing times for the detection of the circle and the cross markers are 105.9 ms and 113.8 ms, respectively. The

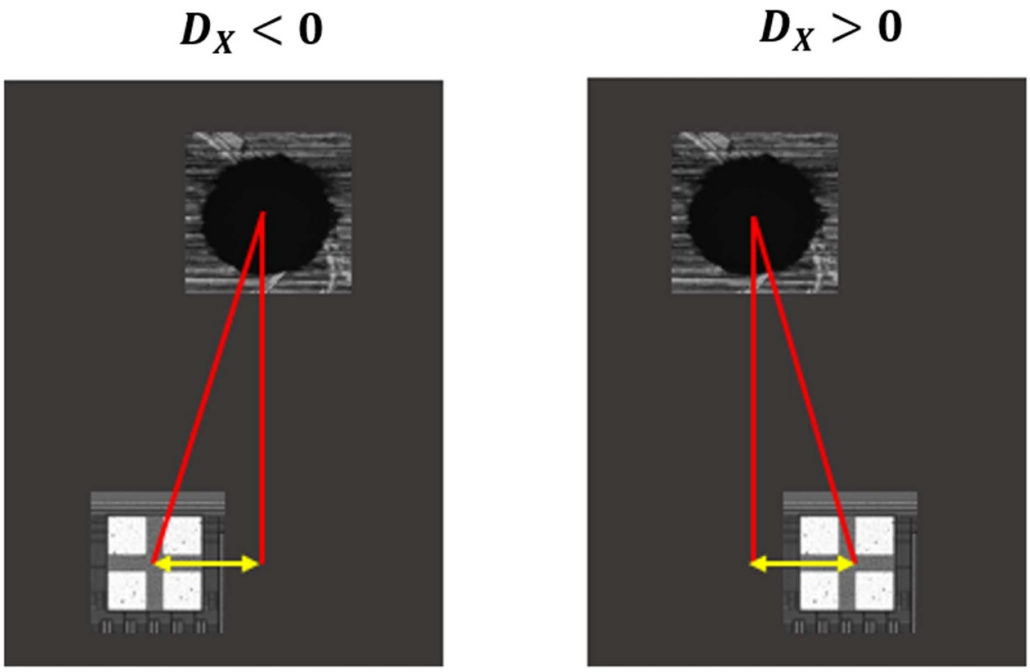

Figure 7. Two possibilities for the D_X sign.

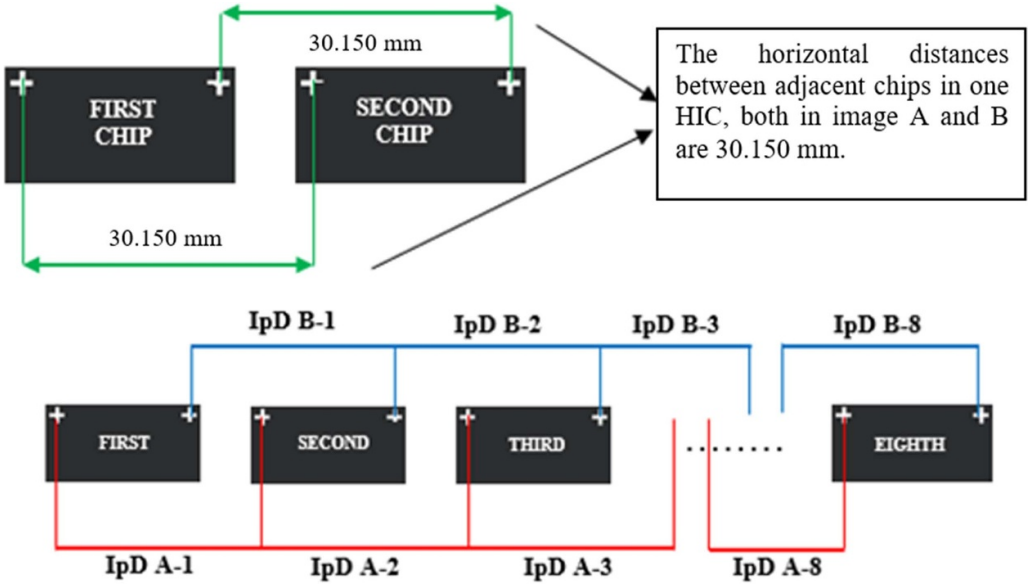

Figure 8. Inter pixel distances.

cross marker that has been detected using the template matching method is highlighted by white dots around it. The brightest white dot in the center represents the object's centroid.

However, even if there is just one actual circle marker, the algorithm can detect some false circles at a particular threshold level in some images, as shown in figure 10. These false circles are due to a poorly detected edge point since the circle marker has a very low gray level in the original image [28].

Table 3 summarizes the D_X and the D_Y values measured for the 9 chips of one HIC. The D_Y values of image A and image B are consistent. As shown in figure 7, there are two possible signs for the D_X values depending on the relative position of the cross and the circle markers. A deviation by up to 20 µm from the nominal position, resulting in values of D_X different from zero, is observed in table 3 left for some chips. These deviations could be due to a misplacement occurring during the gluing process between the FPC and the chip. In addition, imprecision is also a result of the extension area on the chip sealring [11].

Table 4 summarizes the measurement results for the inter pixel distances for HIC E106. It can be seen that there are almost no differences between the measured and the reference

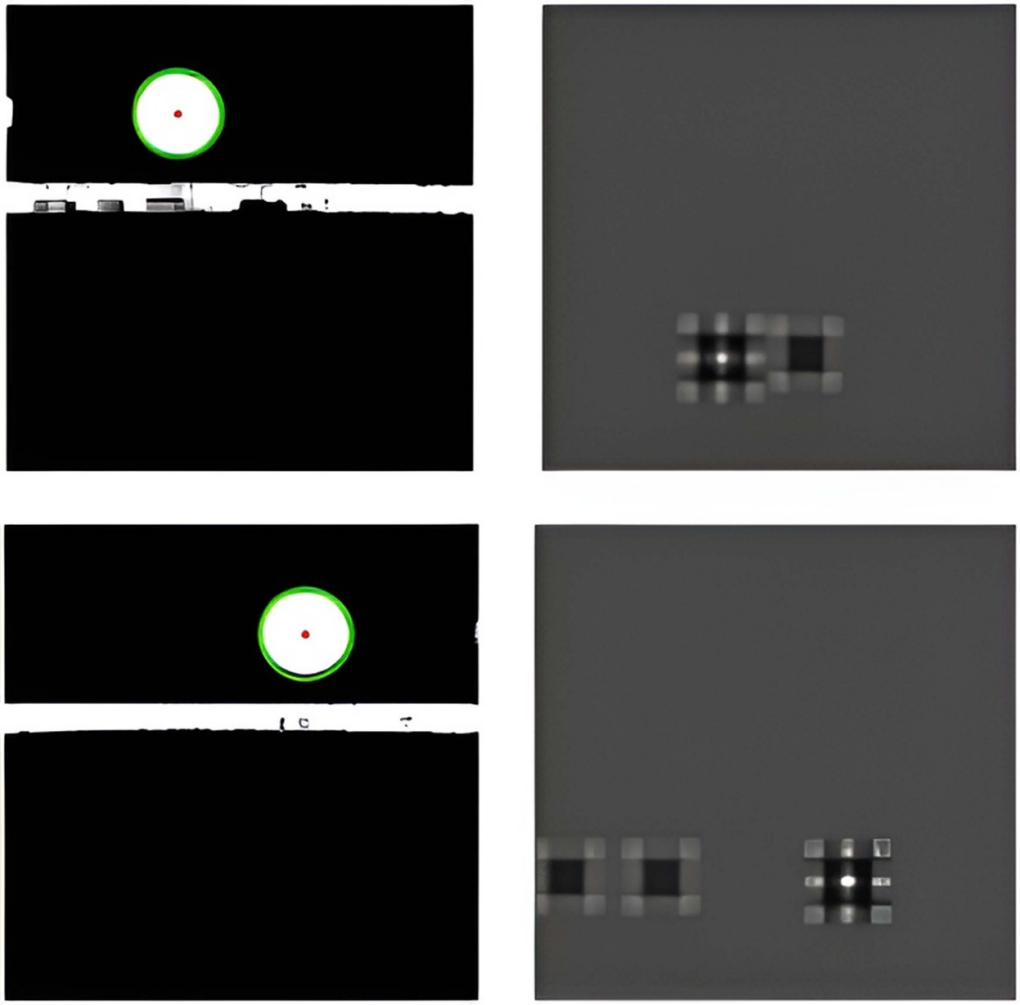

Figure 9. Position of the reference markers as detected by the algorithms.

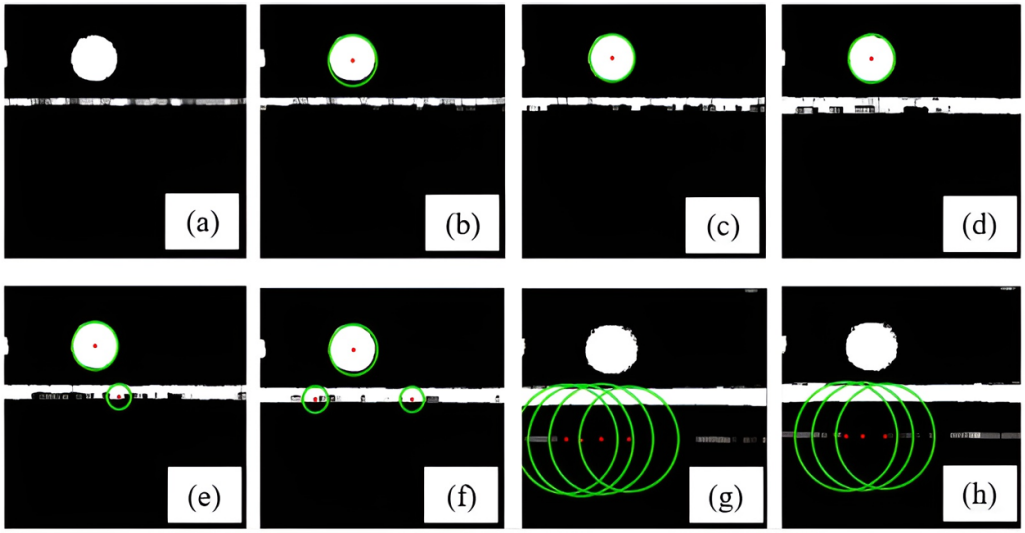

Figure 10. The false circles detected by the algorithm.

Table 3. D_X and D_Y values from image A and image B of one HIC.

CHIP	D_X A (μm)	D_X B (μm)	D_Y A (μm)	D_Y B (μm)
51PK407TA2	19.04	13.60	579.36	576.64
51PK407TA4	21.76	2.72	565.76	568.48
51PK407TA6	8.16	8.16	582.08	576.64
51PK407TA7	8.16	8.16	584.40	582.08
51PK407TB2	5.44	−2.72	584.40	579.36
51PK407TB5	0	5.44	582.08	582.08
51PK407TC2	0	0	579.36	579.36
51PK407TC3	2.72	−5.44	571.20	579.36
51PK407TC5	−5.44	−8.16	584.40	579.36

Table 4. Inter pixel distances of HIC E106.

CHIP	*IpD*	Measured (mm)	Reference (mm)	Deviation (μm)	Relative deviation (%)
51PK407BA1	*IpD* A−1	30.142	30.146	−4	0.0132
	IpD B−1	30.142	30.147	−5	0.0165
51PK407BA3	*IpD* A−2	30.152	30.145	7	0.0232
	IpD B−2	30.155	30.146	9	0.0298
51PK407BA5	*IpD* A−3	30.139	30.153	−14	0.046
	IpD B−3	30.150	30.150	0	0
51PK407BA7	*IpD* A−4	30.150	30.144	6	0.0199
	IpD B−4	30.142	30.147	−5	0.0165
51PK407BB4	*IpD* A−5	30.155	30.149	6	0.0199
	IpD B−5	30.147	30.149	−2	0.0066
51PK407BB6	*IpD* A−6	30.144	30.148	−4	0.0132
	IpD B−6	30.147	30.148	−1	0.0033
51PK407BB7	*IpD* A−7	30.147	30.151	−4	0.0132
	IpD B−7	30.155	30.150	5	0.0165
51PK407BC2	*IpD* A−8	30.169	30.146	23	0.0762

values. The reference values are those provided by the vision system of the MAM, with a precision value of 5 μm. The average deviation between the measured and reference values is 1.13 μm, corresponding to a relative average deviation of 0.021%. The largest deviation is 23 μm, whereas for one chip, a deviation smaller than 1 μm is found. The deviations between measured and reference values for the inter pixel distances of the HIC E106 are shown in figure 11. The measurement deviations relative to the reference values are shown in figure 11(a). There is a chance that the measured value will differ from the reference value in either direction. The histogram in figure 11(a) presents a summary of the deviation values. According to the histogram, the centroid value of the deviations is in close proximity to zero. The data indicates that the measurement deviation falls within the acceptable range of accuracy.

Table 5 summarizes the measurement result from the other 11 HICs that were characterized. The maximum deviation in some HICs is larger than 5 μm, which was not expected. Indeed, for a significant fraction of the chips, the deviations between the measured and reference values are lower than 5 μm. They correspond to cases in which the noise in the image is quite low and the algorithm is able to precisely detect the position of the markers. Instead, the measurements deviating by more than 5 μm from the reference values are mostly cases in which the circle marker in the original image has a very low gray value and a large noise. This affects the determination of the circle marker centroid, and consequently, it biases the measured D_X and D_Y values. The algorithm has a high accuracy value (>99.884%).

Table 6 compares several visual inspection methods for a variety of electrical component-related things. The methods are compared by using four parameters: the observed object, the image resolution, the assessment accuracy, and the processing speed. Unfortunately, most papers do not provide information on image resolution. Method [1] can provide high accuracy and less processing time compared to the method presented in this paper. However, if we add the resolution parameter, our proposed method has more advantages than method [1]. We use images with a more precise scale. Our image is analyzed at a scale of 0.54 μm per pixel, whereas [1] is less precise at 3.45 μm per pixel. Therefore, our method is capable of providing high performance in terms of accuracy and processing speed, although we use a more precise image. Furthermore, the developed algorithm holds potential for defect detection and quality control in electrical components or wafers. However, in order to reduce the occurrence of false circle detections, future enhancements could consider incorporating the gradient method rather than relying solely on the standard Hough transform [28]. The modified method is known as the Gerig-Klein modification to the Hough Transform with Gradient.

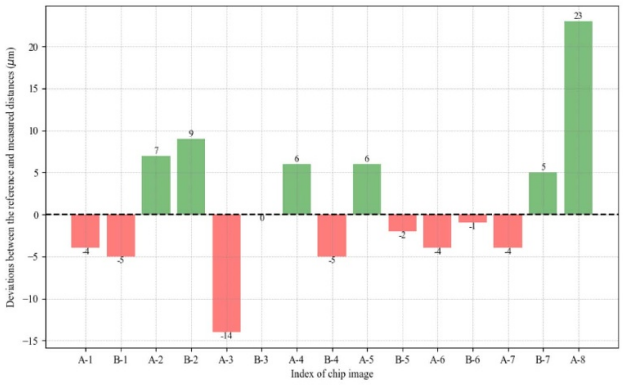

(a) Diagram of upward and downward deviations.

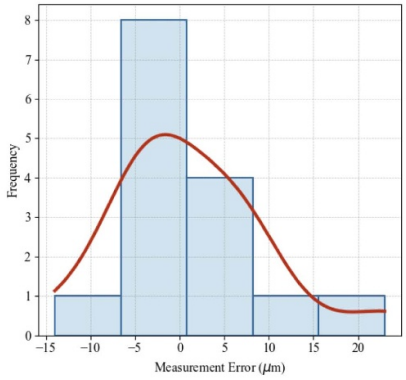

(b) Histogram of the deviations.

Figure 11. The deviations between the reference and measured distances of HIC E106.

Table 5. Inter pixel distances of HIC sample.

HIC	Number of chips	Minimum deviation (μm)	Maximum deviation (μm)	Average deviation (μm)
C003	5	0	6	−1.000
C201	9	1	27	2.867
D105	9	2	35	4.200
E101	9	0	14	1.933
E105	9	1	11	−0.200
E106	9	0	23	1.133
F101	9	1	11	0.133
S001	9	1	31	1.375
S004	9	0	21	−1.438
T003	9	0	30	2.200
U005	9	0	25	1.933
X006	9	1	33	−0.625

Table 6. Comparison of visual inspection methods for microscopic structure.

Reference	Year	Method	Object	Img. Res. (μm/pixel)	Acc.(%)	Speed (s)
[29]	2010	Template matching and 2D DWT	IC wafer	—	—	0.91/*chip*
[30]	2012	Template matching and edge detection	Flexible PCB	—	93.50	0.124/*image*
[31]	2014	Template matching and DWT	Optical IR cut filter	—	96.44	1.05/*sample*
[1]	2018	Template matching	Semiconductor	3.45	99.25	0.08
[32]	2019	CNN and Hough transform	Bottle shape	—	99.60	0.358
[33]	2021	CNN	IC wire bonding	—	93.60	0.078
[13]	2022	Hybrid Classical Quantum CNN	Semiconductor	—	99.00	—
Ours	2023	Hough transform and template matching	Sensor chip	0.54	99.00	0.105/*image*

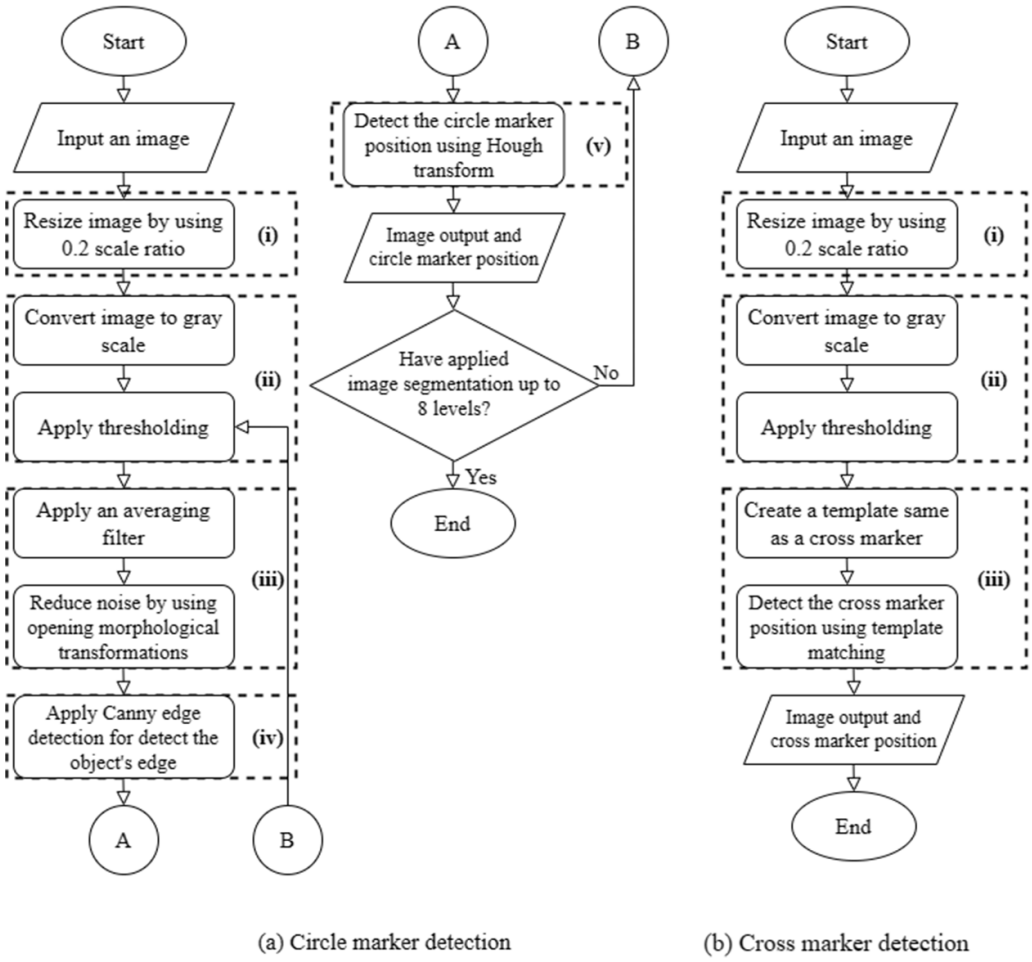

Figure 12. Ablation study scheme.

4.1. Ablation study of the proposed methods

In this section, the additional ablation study has been added. Two proposed algorithms for detecting circle and cross markers are the subject of this study. The ablation procedure utilized in this investigation is depicted in figure 12. The research assesses the individual impact of detection stages on the ultimate outcome. By performing the ablation study, it is possible to identify the most crucial stage in the detection of the chip markers.

4.1.1. Study on circle marker detection. The process of detecting circle markers consists of five primary steps. Simplifying the entire procedure, the steps are categorized into five stages according to their respective substantial contributions. The process for detecting circle markers can be described as follows:

(i) **Image scaling**: This step involves reducing the image size by a scale ratio of 0.2, aimed at enhancing computational efficiency without compromising essential image features.

(ii) **Grayscale conversion and thresholding**: Following image scaling, the image is converted to grayscale and subjected to thresholding to emphasize relevant details while suppressing noise.

(iii) **Filtering**: The averaging filter helps smooth out the image, reducing noise and fine details that may interfere with subsequent processing steps. Morphology opening further aids in noise reduction by removing small objects and fine structures while preserving larger, more significant features. These steps collectively enhance the clarity of the image and improve the accuracy of subsequent processing.

(iv) **Edge detection**: This step is crucial for identifying potential circular shapes, as edges are often indicative of object boundaries. By detecting edges, we prepare the image for circle detection while filtering out irrelevant information.

(v) **Circle detection**: The final step utilizes the Hough transform to robustly detect circular patterns within the processed image. This step completes the circle marker detection process, providing precise localization and characterization of circular objects within the image.

Table 7. Ablation study for marker detection.

Method	Step	Modification	Accuracy	Notes
Circle marker detection	1	Image resizing	99%	Significant difference in processing time observed
	2	Thresholding	99%	Increase in false circles with higher thresholds
	3	Kernel filter modification	99%	No change in accuracy observed
	4	Canny edge detection thresholds	99%	Critical for circle detection; undetected circles if omitted
	5	Hough circle parameters adjustment	Varied	Detection impacted significantly by parameter adjustments
Cross marker detection	1	Image resizing	99%	Consistent results observed
	2	Thresholding	99%	No significant impact on accuracy
	3	Template matrix adjustment	Varied	Accuracy drop observed for *IpD* B; deviations from original cross marker structure observed

To assess the significance of each step, we conduct experiments by selectively removing individual components while retaining others. A comparative analysis is performed to evaluate the impact on detection accuracy and computational efficiency.

4.1.2. Study on cross marker detection. The ablation study for cross marker detection, as explained in the previous section, is also conducted by evaluating the contribution of each algorithm step. The primary stages involved in cross marker detection are outlined below.

(i) **Image scaling**: Similar to circle marker detection, image scaling is employed to reduce the computational burden while preserving essential image features.
(ii) **Grayscale conversion and thresholding**: Grayscale conversion and thresholding are performed to simplify image representation and enhance feature extraction.
(iii) **Template creation and matching**: Cross marker detection involves the creation of a template representing the characteristics of a cross marker, followed by template matching to identify potential cross marker positions.

As with circle marker detection, an ablation study is conducted to assess the individual contributions of each step in the cross marker detection algorithm. Comparative analysis is conducted by systematically removing and reintroducing components to evaluate their impact on detection performance.

4.1.3. Experimental results of the ablation study. Experimental results from the ablation study demonstrate the effectiveness of the proposed methods for both circle and cross marker detection. Through a quantitative analysis of detection accuracy and computational efficiency, we elucidate the significance of each step in the detection algorithms. Additionally, qualitative assessments are provided to illustrate the impact of individual components on the detection results.

Table 7 summarizes that in our study, we systematically enhanced the efficiency and accuracy of our proposed method for detecting both circle and cross markers. We focus primarily on circle marker detection and conduct a series of ablation experiments. Firstly, we resize the images using scaling factors of 0.5 and 1.0. Remarkably, despite variations in processing time, the accuracy remains consistently high at 99%. However, it is important to note that as the scaling factor increases, more false circles are detected. Next, we fine-tune the threshold levels to maintain the same accuracy. Although this adjustment ensures robust performance, it also leads to more false circles being detected due to higher threshold values. We explore modifications to the kernel filter size, but interestingly, these changes do not significantly impact the accuracy. Additionally, we find that adjusting the Canny edge detection thresholds and the Hough circle parameters is crucial for circle detection.

Similarly, for cross marker detection, resizing the image and modifying thresholding levels maintained stable accuracy. We investigate the effects of modifying matrix templates on the accuracy of image processing algorithms. Specifically, we scaled down the template values by a factor of 0.5 and increased them by a factor of 2. Our findings reveal that while the accuracy for *IpD* A remains consistent at 99%, the accuracy for *IpD* B experiences a drastic decline to approximately 88%. Additionally, the resulting output images do not align well with the original cross marker. The critical step identified for cross marker detection was step 3, indicating the significance of adjusting the template matrix size for accurate detection, particularly for *IpD* B.

First, the normal template size was set at 41×41 pixels, as shown in figure 13(a). Figure 13(b) demonstrates the outcomes after scaling up the template values, resulting in a size of 82×82 pixels, while figure 13(c) depicts the results following a scaling down of the template values , resulting in a size of 20×20 pixels. Notably, the choice of scaling factor significantly influences the accuracy of template matching algorithms, underscoring the importance of careful selection in image processing tasks.

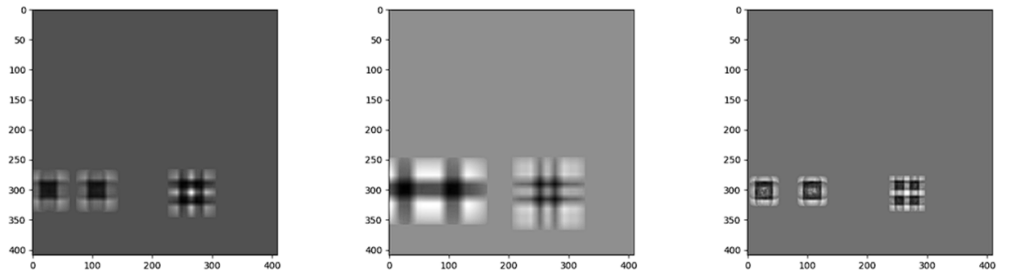

(a) Normal (b) Scaled up by a factor of 2 (c) Scaled down by a factor of 0.5

Figure 13. Template size affects the accuracy of marker detection.

5. Conclusions

The developed algorithm can be used to detect the positions of the circle and the cross markers on the ALPIDE sensor chip. The algorithm is supported by combining two detection algorithms, namely circle and cross marker detection. The detection results are used to validate that the sensor position follows the detector manufacturing standard. The accuracy of the proposed method is better than 99%. The outcomes show that the developed algorithm is able to verify the precision of the sensor alignment. The algorithm is also able to provide fast analysis. The average processing times for the circle and the cross markers detection are 105.9 ms/image and 113.8 ms/image, respectively. The ablation study finds the crucial contribution of some algorithmic steps. The edge detection and Hough transform make a significant contribution to obtaining the circle marker. Meanwhile, the dominant parameter for cross marker detection is the template size. The developed algorithm might be used for defect detection and quality control on electrical components or wafers. This research work could be improved in the future, especially on circle detection. The Gerig–Klein modification to the Hough Transform with Gradient may have the capacity to be implemented. This approach may reduce the false circle detection. In contrast to the existing approach, which solely relies on the conventional Hough transform. The shape and template dimension of the pattern could vary depending on the texture of the observed objects. Appropriate preprocessing techniques are required to enhance the image intensity and reduce the large noise.

Data availability statements

The data cannot be made publicly available upon publication because they are owned by a third party and the terms of use prevent public distribution. The data that support the findings of this study are available upon reasonable request from the authors and CERN approval.

Acknowledgments

We would like to thank Francesco Prino for his contribution to reviewing the manuscript draft. The research is part of the collaboration between the Indonesian National Research and Innovation Agency (BRIN) and CERN. The research activities of Indonesian researchers were fully supported by BRIN. The Research and Innovation in Science and Technology Project (RISET-Pro) program (No. 225/D.D3/KPT/2019) funded the research visit of Indonesian researchers to CERN in 2019. The image data is obtained based on the collaboration between BRIN and CERN. The authors acknowledge the support of CERN in ensuring this paper is freely accessible through open access publication.

ORCID iDs

Ahmad Satya Wicaksana https://orcid.org/0009-0005-4516-0336
Esa Prakasa https://orcid.org/0000-0003-4685-6309

References

[1] Chen F, Ye X, Yin S, Ye Q, Huang S and Tang Q 2018 Automated vision positioning system for dicing semiconductor chips using improved template matching method *The Int. J. Adv. Manuf. Technol.* **100** 2669–78
[2] Zhu W, Gu H and Su W 2020 A fast PCB hole detection method based on geometric features *Meas. Sci. Technol.* **31** 095402
[3] Shen X, Xing Y, Lu J and Yu F 2023 Detection of surface defect on flexible printed circuit via guided box improvement in ga-faster-rcnn network *PLoS One* **18** e0295400
[4] Zheng J, Sun X, Zhou H, Tian C and Qiang H 2022 Printed circuit boards defect detection method based on improved fully convolutional networks *IEEE Access* **10** 109908–18
[5] Zhou Y, Yuan M, Zhang J, Ding G and Qin S 2023 Review of vision-based defect detection research and its perspectives for printed circuit board *J. Manuf. Syst.* **70** 557–78
[6] Yeum C M and Dyke S J 2015 Vision-based automated crack detection for bridge inspection *Comput.-Aided Civil Infrastruct. Eng.* **30** 759–70
[7] Nayak J P, Anitha K, Parameshachari B, Banu R and Rashmi P 2017 Pcb fault detection using image processing *IOP Conf. Ser.: Mater. Sci. Eng.* **225** 012244
[8] Zhang M and Xi H 2023 Detection algorithm of surface defect word on printed circuit board *Comput. Syst. Sci. Eng.* **46** 3911–23
[9] Nan G and Gao Y 2018 Automated visual inspection of multipattern train components using gradient information

and feature fusion under the illumination-variant condition *Proc. Inst. Mech. Eng.* F **232** 1500–13
[10] Kumar S, Kumar Upadhyay A, Dubey P and Varshney S 2021 Comparative analysis for edge detection techniques *Int. Conf. on Computing, Communication, and Intelligent Systems (ICCCIS)* (*Greater Noida, India*, *19–20 February 2021*) pp 67–81
[11] Panjaitan G, Lhaksmana K, Prakasa E and Musa L 2019 Detecting the position of the sealring and the edge on the sensor chip *J. Phys.: Conf. Ser.* **1192** 012063
[12] Tsai D-M and Huang C-K 2019 Defect detection in electronic surfaces using template-based fourier image reconstruction *IEEE Trans. Compon. Packag. Manuf. Technol.* **9** 163–72
[13] Yang Y-F and Sun M 2022 Semiconductor defect detection by hybrid classical-quantum deep learning *2022 IEEE/CVF Conf. on Computer Vision and Pattern Recognition (CVPR)* (*New Orleans, LA, USA*, *18–24 June 2022*) pp 2323–32
[14] Zheng X, Zheng S, Kong Y and Chen J 2021 Recent advances in surface defect inspection of industrial products using deep learning techniques *Int. J. Adv. Manuf. Technol.* **113** 35–58
[15] Tsalicoglou C and Rösgen T 2022 Deep learning based instance segmentation of particle streaks and tufts *Meas. Sci. Technol.* **33** 114005
[16] Schlosser T, Friedrich M, Beuth F and Kowerko D 2022 Improving automated visual fault inspection for semiconductor manufacturing using a hybrid multistage system of deep neural networks *J. Intell. Manuf.* **33** 1099–123
[17] Jia Z, Wang M and Zhao S 2023 A review of deep learning-based approaches for defect detection in smart manufacturing *J. Opt.* **26** 013001
[18] Apostolopoulos I D and Tzani M A 2023 Industrial object and defect recognition utilizing multilevel feature extraction from industrial scenes with deep learning approach *J. Ambient Intell. Hum. Comput.* **14** 10263–76
[19] Ren Z, Fang F, Yan N and Wu Y 2022 State of the art in defect detection based on machine vision *Int. J. Precis. Eng. Manuf.-Green Technol.* **9** 661–91
[20] Cai G and Gong L 2020 Machine vision based segmentation of the goldplate area from a flexible printed circuit board *2020 2nd Int. Conf. on Artificial Intelligence and Advanced Manufacture (AIAM)* (*Manchester, United Kingdom*, *15–17 October 2020*) pp 340–4
[21] Chen S, Liang X and Jiang W 2023 PCB defect detection based on image processing and improved YOLOV5 *J. Phys.: Conf. Ser.* **2562** 012002
[22] Szu-Yin L and Hao-Yu L 2021 Integrated circuit board object detection and image augmentation fusion model based on YOLO *Front. Neurorobot.* **15** 762702
[23] Liu C, Zhou X, Li J and Ran C 2023 PCB board defect detection method based on improved yolov8 *Front. Comput. Intell. Syst.* **6** 1–6
[24] Mauro A Di *et al* (A. Collaboration) 2019 The new inner tracking system for the ALICE upgrade at the LHC *Nucl. Instrum. Methods Phys. Res.* A **936** 625–9
[25] Wardoyo S, Firmansyah T, Prima N, Wiyono W, Soenarto S and Mardapi D 2020 Vertebra osteoporosis detection based on bone density using index-singh statistical blended method *Telkomnika* **18** 148
[26] Dhruv B, Mittal N and Modi M 2017 Analysis of different filters for noise reduction in images *2017 Recent Developments in Control, Automation & Power Engineering (RDCAPE)* (*Noida, India*, *26–27 October 2017*) (IEEE) pp 410–5
[27] Zhang J, Li C, Rahaman M M, Yao Y, Ma P, Zhang J, Zhao X, Jiang T and Grzegorzek M 2022 A comprehensive review of image analysis methods for microorganism counting: from classical image processing to deep learning approaches *Artif. Intell. Rev.* **55** 2875–44
[28] Yuen H, Princen J Illingworth J and Kittler J 1990 Comparative study of hough transform methods for circle finding *Image Vis. Comput.* **8** 71–77
[29] Liu H, Zhou W, Kuang Q, Cao W and Gao B 2010 Defect detection of ic wafer based on two-dimension wavelet transform *Microelectron. J.* **41** 171–7
[30] Liao C-T, Lee W-H and Lai S-H 2012 A flexible pcb inspection system based on statistical learning *J. Signal Process. Syst.* **67** 279–90
[31] Liu Y and Yu F 2014 Automatic inspection system of surface defects on optical ir-cut filter based on machine vision *Opt. Lasers Eng.* **55** 243–57
[32] Wang J, Fu P and Gao R 2019 Machine vision intelligence for product defect inspection based on deep learning and hough transform *J. Manuf. Syst.* **51** 52–60
[33] Chen J, Zhang Z and Feng W 2021 A data-driven method for enhancing the image-based automatic inspection of ic wire bonding defects *Int. J. Prod. Res.* **59** 4779–93